Rare Metal Materials and Engineering
Volume 50, Issue 5, May 2021
Available online at www.rmme.ac.cn

Science Press

Cite this article as: Feng Ruicheng,Qi Yongnian,Li Haiyan,et al.Acoustic Emission Response to Brittle Cutting of 6H-SiC Using Molecular Dynamics[J].Rare Metal Materials and Engineering, 2021, 50(05): 1602-1610.

ARTICLE

Acoustic Emission Response to Brittle Cutting of 6H-SiC Using Molecular Dynamics

Feng Ruicheng[1,2], Qi Yongnian[1,2], Li Haiyan[1,2], Song Wenyuan[1,2], Fan Lihe[1,2], Lei Chunli[1,2], Feng Guojin[3], Rui Zhiyuan[1,2]

[1] School of Mechanical and Electrical Engineering, Lanzhou University of Technology, Lanzhou 730050, China; [2] Key Laboratory of Digital Manufacturing Technology and Application, Ministry of Education, Lanzhou University of Technology, Lanzhou 730050, China; [3] Centre for Efficiency and Performance Engineering, University of Huddersfield, Huddersfield HD1 3DH, UK

Abstract: The acoustic emission (AE) response to brittle cutting of 6H-SiC was studied by molecular dynamics simulation. The micro-deformation and crack formation at atomic scale were analyzed. Furthermore, the AE sources in machining were distinguished and their corresponding AE characteristics were discussed. The results show that the brittle deformation process of 6H-SiC at cutting depth of 77 nm is simple but unusual. The deformation possesses discontinuous dislocation propagation and divides the deformed workpiece into pieces, and then the crack is initiated from a fast dislocation propagation. The compressive stress results in the decline of AE power initially. Three AE sources clustered in the frequency-energy analysis are lattice vibration, dislocation propagation and crack propagation. In addition, the AE response of two times of dislocation propagation shows a higher frequency characteristic than lattice vibration does at temperature of 1 K, with the lowest energy occupation in total. On the contrary, the AE response of crack propagation has apparent frequency and energy accumulation characteristics.

Key words: acoustic emission; brittle machining; 6H-SiC; molecular dynamics

As an ultra-precision machining methods, nano-cutting[1] obtains high quality surface by removing a few layers of atoms on the target sample. Due to its inherent advantages, such as efficiency, low-cost and large dimension span, nano-cutting has been widely applied in industries, such as semiconductors, optics, aerospace, and military applications. To control the surface quality and surface residual stress, it is of great importance to monitor the cutting conditions, such as tool wear[2], early warnings of crack initiation[3] and brittle-ductile transition (BDT)[4] of the cutting. Acoustic emission (AE)[5] is the rapid release of the local strain energy by sound wave emission. As a non-destructive method discovered in 1950s, AE has been successfully applied in the industries of pipelines, airplanes, refineries, manufacturing, etc. Recently, researchers showed that AE can also be utilized as an effective online method to monitor the cutting process.

A comprehensive exploration of AE sources helps understand the deformation behavior and the cutting conditions. According to the review of Vinogradov[6], the sources of AE in nano-cutting come from many aspects, among which the dislocation activities are the main sources of AE. Eshelby[7] proved that the sound radiation is from the edge dislocations oscillating near the equilibrium position, indicating that the weak AE comes from dislocations. The dislocation annihilation on the surface is one of the main AE sources. Merson et al[8] studied the AE in the deformation process of copper with different ratios of surface area and volume, and the results showed that AE is proportional to the surface area. Hora et al[9] implied that the dislocation motion near surface layer can be accelerated by image force at subsonic speed[10], which is symmetric to the free surface, and the results indicated that the surface tension facilitates the dislocation annihilation at free surface. Besides, Vinogradov[6] pointed out that the AE peak can be only observed with the deformation of near-surface layer of metal. Also, the dislocation slip and the formation of twin dislocation are the main sources of AE. Vinogradov et al[11] analyzed the

Received date: October 24, 2020
Foundation item: National Natural Science Foundation of China (52065036); Natural Science Foundation of Gansu (20JR5RA448); Hongliu First-class Disciplines Development Program of Lanzhou University of Technology
Corresponding author: Qi Yongnian, Master, School of Mechanical and Electrical Engineering, Lanzhou University of Technology, Lanzhou 730050, P. R. China, E-mail: yunai2384@163.com

AE response to the activities of dislocation slip and twinning in the cyclic deformation of pure Mg, and the results well agreed with the in-situ observations. However, the twinning is not likely to be the main source in nano-cutting. Zhu et al[12] studied the twinning deformation in face centered cubic (fcc) nanocrystalline metals and found that with the decrease of grain size, the formation of twin is easier, but becomes more difficult at nano scale. Besides, the phase transformation is also the main source of AE, which can accommodate the plastic deformation in addition to dislocation slip. Müller et al[13] conducted the tensile tests of cast steel, and found that the AE cluster of martensitic phase transformation at the yielding point is significantly influenced by the deformation temperature. In recent years, combining with the molecular dynamics (MD) methods, the acoustic emission from individual defects[14] and the dislocation motion near surface[9] are directly depicted and analyzed. The dislocation motion and propagation in the nanoindentation of single crystal copper was studied by Nikonov et al[14] to imply its influence on the AE signal, and the results showed that the dislocation motion and propagation does not produce pronounced peaks on the signal.

During the cutting process of brittle materials, the brittle fracture always originates from the micro crack of machined surface by brittle cutting mode, which degrades the mechanical strength of products, such as silicon and germanium. The activities of dislocations are conducive to the plasticity of metals. Besides, the brittle fracture usually happens under high pressure when the dislocation-starvation occurs. Regarding the cutting process, ductile mode cutting can prevent cracks from the cutting surface or subsurface, and the precise control of BDT of cutting mode is thereby necessary for controlling cracks in machining.

The 6H-SiC, which is a kind of the ceramics, has about half hardness of the diamond and has been applied in the semiconductor manufacturing. The brittle mode machining degrades the performance of product dramatically, so the ductile machining control is necessary. The stacking sequence of 6H-SiC is ABCACB. 6H-SiC attracts attention for its thermal shock resistance, high chemical inertness and high thermal conductivity[15]. However, the sp^3 orbital hybridization and tetrahedral covalent bonds make it more susceptible to form cracks during machining and result in brittle fracture. In the study of ductile deformation machining of 6H-SiC, Xiao et al[16] identified that the quantity of high pressure phase transformation (HPPT) is quite small, the dislocation plays a major role in the ductile cutting region, and the amorphous phase does not significantly produce by Raman spectroscopy analysis. Meng et al[17] performed nano-scratch tests on 6H-SiC and found that the critical depth of BDT is around 75 nm when the applied normal load is about 12.2 mN. Besides, Meng et al[18] simulated the nano-cutting of 6H-SiC along different crystal orientations, and the dislocation on slip system (0001) prevails when the cutting plane and direction is (0001). Li et al[19] performed irradiation of He^+ ions upon 6H-SiC single crystal before annealing. The damaged bands were initially observed in the irradiated area at 400 ℃, and then the damage evolved from plate-shaped bubble to pits and cracks with increasing the annealing temperature. Apart from the 6H-SiC, 3H-SiC and 4H-SiC are two forms of SiC, which are widely used in the semiconductor products. Xiao et al[20] compared the two contradictory statements: (1) Noreyan et al proposed that the high pressure phase transformation was responsible for the ductile response of 3H-SiC in the nanoindentation[21] and nano-scratching[22] tests; (2) Yan et al[23] investigated and believed that the dislocation activities are response for the ductile response of 3H-SiC. Xiao et al[20] validated that both the high pressure phase transformation and dislocation activities are responsible for the ductile response of 3H-SiC, while the dislocation activities play a major role. Geng et al[24] tested the nano-scratching on monocrystalline germanium, and the critical depth of BDT is around 561 nm.

From the view of the nature of AE, it is capable to detect defects at nano scale, and extensive tests in different scales have proven that AE signal is sensitive enough for detecting defects even at nanometric scale. Deschanel et al[3] predicted the crack propagation in the early stage using AE method. Lee[25] confirmed the feasibility of detecting AE signals from the structural change of single crystal silicon by nanometric machining based on atomic force microscope (AFM), and the results showed that response of AE to the BDT with critical depth of 35 nm agrees well with theoretical value. However, the details of AE sources, such as dislocation motion or phase transformation derived from experiment, may be severely affected by the white noise, and the direct detection of AE inside the metals is impossible because the sensor is tied on the surface of specimen, which makes the sensor more sensitive to the strain of surface.

As a supplement to the experiments, MD method can easily avoid the electronic noises and impurities of specimen. The energy of AE rapidly decreases with the log of distance, and only the AE from dislocation movement needs to be further investigated because the sensors located on the surface are more sensitive to the strain on the surface. In addition, the experimental investigation of the AE inside the workpiece can bring details for THz frequency and the motion of dislocations.

In this study, the simulation of ductile machining of 6H-SiC was carried out to investigate AE at nano scale. Nano cracks and dislocations in cutting process were studied with their AE response in detail. The simulation, methods of spectral analysis, the results of simulation and spectral analysis were discussed.

1 Methods

1.1 MD simulation

1.1.1 Simulation model

As shown in Fig.1, the model contains workpiece with ~1 600 000 atoms, and the related cutting process parameters are listed in Table 1. The cutting tool was modeled as nondeformable body, and the periodic boundary condition was adopted along *Z* direction. The workpiece was divided into three layers: (1) Newtonian layer, which performs the Newton's

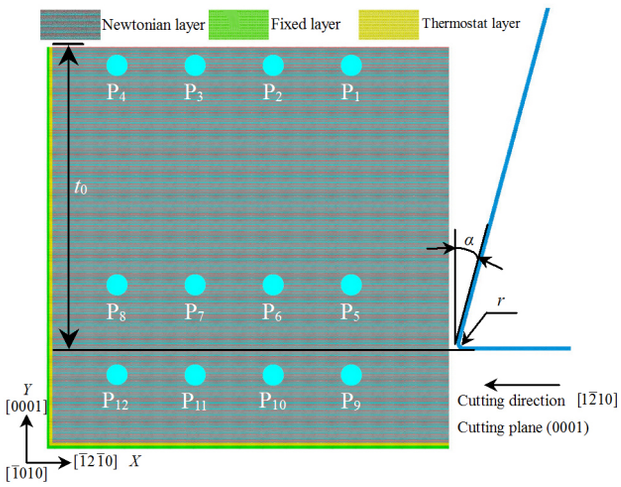

Fig.1 Schematic diagram of cutting model with data collecting points

Table 1 Cutting process parameters

Parameter	Value
Cutting tool material	Single crystal diamond
Workpiece dimension (L_1×L_2×L_3)	100 nm×100 nm×1.6 nm
Tool edge radius, r/nm	2
Uncut chip thickness, t_0/nm	77
Rake angle, α/(°)	15
Cutting speed/nm·ps^{-1}	0.05
Cutting direction and plane	[1$\bar{2}$10](0001)
Timestep/fs	1
Temperature/K	1
Data collecting points	P_i (i=1, 2, ⋯, 12)

second law between atoms; (2) fixed layer, which prevents the atoms from moving out of boundary by locating at the bottom and left end of workpiece; (3) thermostat layer, which locates between the two mentioned layers to absorb dispersed heat during cutting. The simulation was carried out with the constant of *NVT* ensemble, where *N*, *V*, *T* indicate the number of atoms, the volume and the temperature, respectively. The Nosé-Hoover thermostat was used to exchange energy with thermostat layer atoms to keep the constant temperature, and the system was equilibrated with the thermostat at 1 K for 90 ps.

1.1.2 Structure of 6H-SiC

The cell structure of 6H-SiC is shown in Fig. 2a and 2b, and the crystal constant for a (a=b) and c is 0.3095 and 1.5185 nm, respectively. The stacking sequence along c axis is ABCACB. As shown in the Fig. 2c, the slip systems of hexagonal crystal in 6H-SiC include basal <a> slip {0001}<11$\bar{2}$0>, prismatic <a> slip {1$\bar{1}$00}<11$\bar{2}$0>, pyramidal <a> slip {10$\bar{1}$1}<11$\bar{2}$0> and pyramidal <c+a> slip {11$\bar{2}$2}<11$\bar{2}$3>. In addition, the two types of dislocations with Burgers vector [$\bar{1}$100] are a combination of two vectors, 1/3[$\bar{1}$2$\bar{1}$0] and 1/3[$\bar{2}$110], and the existence of [$\bar{1}$100] found by X-ray diffraction was stable[26]. Besides, the [$\bar{1}$100] type dislocation partly dominates the plastic deformation of 6H-SiC during the brittle cutting process.

1.1.3 Simulation procedure

The MD simulation was carried out using large-scale atomic/molecular massively parallel simulator (LAMMPS)[27], and the calculation of the second order stress tensor of atom i was from the virial stress components $\sigma_{\alpha\beta}^{ij}$[28,29], which is defined as Eq.(1):

$$\sigma_{\alpha\beta}^{ij} = \frac{1}{\Omega_i}\left[-m_i v_{i\alpha} v_{i\beta} + \frac{1}{2}\sum\nolimits_{j(j\neq i)} x_\alpha^{ij} f_\beta^{ij}\right] \quad (1)$$

where Ω_i is the volume of atom i; m_i is mass of atom i; $v_{i\alpha}$ and $v_{i\beta}$ are velocities of atom i along the direction α and β, respectively; x_α^{ij} and f_β^{ij} are the distance and force between atom i and j along the direction of α and β, respectively. Then the second-order stress tensor is given as follows:

$$\sigma_{ij} = \begin{pmatrix} \sigma_{11} & \sigma_{12} & \sigma_{13} \\ \sigma_{21} & \sigma_{22} & \sigma_{23} \\ \sigma_{31} & \sigma_{32} & \sigma_{33} \end{pmatrix} \quad (2)$$

Voronoi algorithm[30] is a method to calculate the instantaneous volume of atoms. In this study, it performed for the calculation of atom volume as the output stress is in unit of volume×pressure. Thus, the interaction in severely deformed region between the workpiece atoms and the cutting tool atoms can be described precisely.

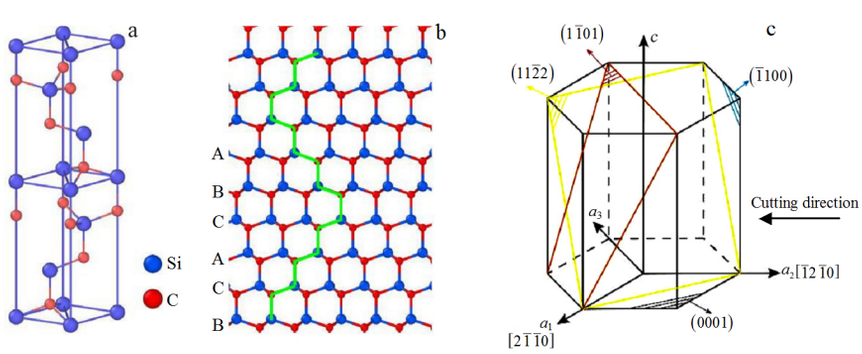

Fig.2 Schematic diagram of cell structure (a), stacking sequence (b), slip systems of hexagonal crystal (c) of 6H-SiC

1.1.4 Interatomic potential energy function

Potential energy function is the function of potential energy and distance between atoms. The Vashishta potential was adopted in modelling elastic properties and deformation behavior of 6H-SiC[31]. The brittle fracture and HPPT were well presented in Ref. [16], and the total potential energy $U_{\text{Vashishta}}$ of system including two-body term V_{ij} and three-body term V_{ijk} is given as follows:

$$U_{\text{Vashishta}} = \sum_{i<j} V_{ij}^{(2)}(r_{ij}) + \sum_{i,j<k} V_{ijk}^{(3)}(r_{ij}, r_{ik}, \cos\theta_{ijk}) \quad (3)$$

where r_{ij} is the distance between atom i and j, i.e., $r_{ij}=r_i-r_j$ and r_i is the position of atom i; $\cos\theta_{ijk}=r_{ij}r_{ik}/(r_{ij}r_{ik})$. But the interaction potential between C atoms was not stable for diamond structure, and the Morse potential was adopted for the interaction between C atoms in the cutting tool and (C, Si) atoms in workpiece. The Morse potential can be described as follows:

$$U_{\text{Morse}}(r_{ij}) = D(\mathrm{e}^{-2\alpha(r_{ij}-r_0)} - 2\mathrm{e}^{-\alpha(r_{ij}-r_0)}) \quad (4)$$

where D is the cohesive energy, α is the inverse length scaling factor and r_0 is the equilibrium distance of atoms. D, α and r_0 for C atoms between the tool and workpiece are 0.18 eV, 0.0455 nm^{-1}, 0.28 nm[32], respectively. D, α and r_0 for interaction between Si atoms of workpiece and C atoms of tool are 0.435 eV, 46.487 nm^{-1}, 0.194 75 nm[33,34], respectively.

The structure was visualized by OVITO open source software[35], and dislocation was extracted by hexagonal diamond (Wurtzite) method in dislocation extraction algorithm (DXA)[36] of OVITO.

1.2 MD simulation

Since AE behaves in the form of stress waves, the AE signal was extracted by a statistical average of stress in a sphere at the points P_i (i = 1, 2, ⋯, 12), which is defined by Eq.(5):

$$\bar{\sigma} = \frac{(\sigma_{11} + \sigma_{22} + \sigma_{33})}{3} \quad (5)$$

The procedure of AE data processing is shown in Fig. 3. Firstly, 40 000 points of AE signals were divided into consecutive individual frames, and there was no overlapping between two continuous frames. Secondly, for each frame i, the power spectral density (PSD) function $G_i(f)$ was calculated using the Welch method. Thirdly, the AE power E and the median frequency f_m were calculated by Eq.(6) and Eq.(7), respectively. And the normalized PSD functions was calculated by Eq.(8). It should be noted that different AE signals from the single source have unique waveform and PSD functions[6].

$$E = \int_{f_{\min}}^{f_{\max}} G(f)\,\mathrm{d}f \quad (6)$$

$$\int_0^{f_m} G(f)\,\mathrm{d}f = \int_{f_m}^{\infty} G(f)\,\mathrm{d}f \quad (7)$$

$$\tilde{G}(f) = G(f)/E \quad (8)$$

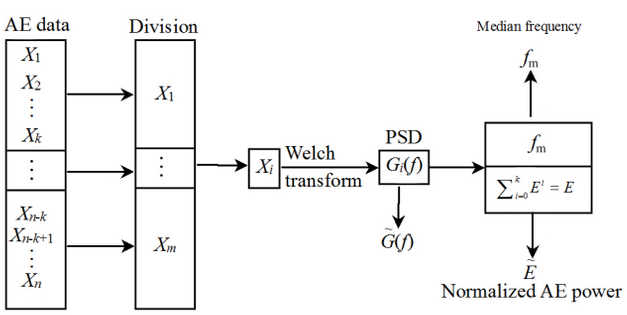

Fig.3 Schematic diagram of AE data processing

2 Results and Discussion

2.1 Crack formation induced by brittle machining

The crack formation process of brittle cutting with 4 timesteps is shown in Fig. 4. The stress coloring of atoms of dislocation propagations (DPs) during the brittle cutting can be seen clearly, as well as the dislocation distribution without workpiece atoms.

The elastic deformation was processed transiently for about 10 ps on the touch between the tool and workpiece. As shown in Fig. 4a and 4b, at timestep of 183 ps, the DP begins under the compressive stress along X axis tilted of about −60º, and then the first possible crack site (PCS) forms subsequently. The dislocation is numbered in sequence, as shown in Fig. 4a, 4d, and 4g. As shown in Fig. 4c, it can be seen that the overall shape of dislocation 1 or 3 is consistent with the shape of the tool, meaning that the deformation degree of the workpiece is induced by the tool shape and the dislocation 1 or 3 on basal plane dominates the deformation process. Dislocation 2 occurs at 233 ps, as shown in Fig. 4d. As a supplement of dislocation 1, dislocation 2 accommodates the deformation part of workpiece below dislocation 1 along the same direction. It is worth noting that the dislocation 2 begins to form at 172 ps and some trails at 233 ps still can be distinguished in Fig. 4e. As a result of the two timesteps of DPs, the part of workpiece ahead of the tool is divided into three pieces, facilitating the formation of dislocation 3 not along the direction of dislocation 1, which is important to interpret the brittle fracture of 6H-SiC. After suffering the compressive stress, the dislocation 3 in Fig. 4d propagates backwards along an opposite direction of dislocation 2 in X axis, and the second PCS forms after several picoseconds. It can be inferred that the back propagation of dislocation 3 is related with the symmetry of 6H-SiC crystal along Y axis. Besides, compared with Fig. 4b and 4h, a higher level of compressive stress distribution in Fig. 4e occurs, which can be concluded that the backward propagation of dislocation 3 only occurs when the propagation of dislocation along direction of dislocation 1 is hard and a higher compressive stress exists.

The second PCS at 233 ps is about to expand just right ahead of the tool. However, the crack does not form there for some reasons. Firstly, as shown in Fig. 4e, the yellow-colored atoms are more than those in other subpictures, which indicates the existence of a larger deformation degree. Secondly, the undeformed atoms escaping from three times of DPs suffer from an increasing strain along Y axis, i.e., the dislocation 4 is generated before the crack formation. As shown in Fig. 4, at 240 ps, the final DP before crack formation (dislocation 4) forms after the dislocation 3 forms and the second PCS disap-

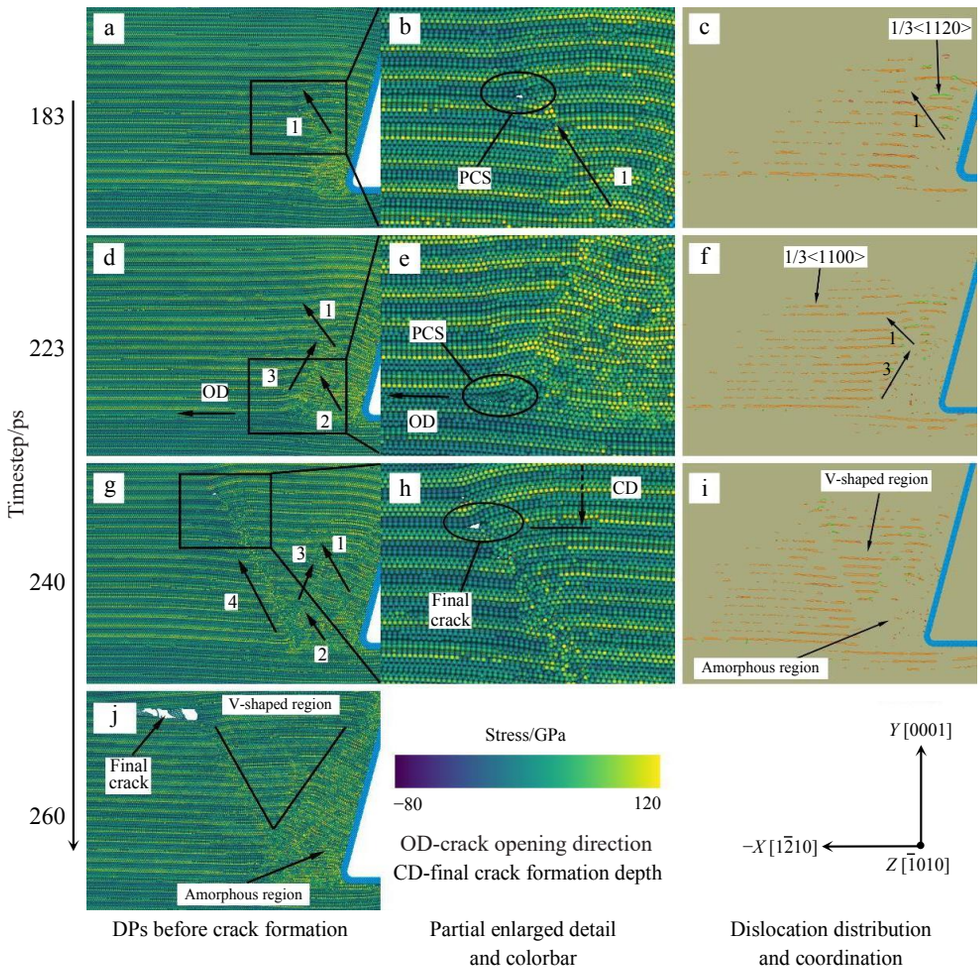

Fig.4 Images of original (a, d, g, j) and partially enlarged (b, e, h) dislocation propagations before crack formation during brittle cutting; dislocation distribution without workpiece atoms of crack formation (c, f, i)

pears under compressive stress. The dislocation 4 grows rapidly to 26 nm in 7 ps, i.e., the growth rate is 26 km/s. At the same time, the final crack forms, as shown in Fig. 4h. The front part of workpiece is divided into several pieces after DPs, and then compressed into the amorphous state, as shown in the dislocation-starvation area in Fig.4c, 4f, and 4i. Besides, the evident propagation of the final crack at 260 ps is shown in Fig. 4j, and the V-shaped region caused by several times of DPs removes due to the expanding of the final crack.

It is reported that the critical cutting depth of BDT is 75 nm with the applied load of 12.2 mN[17], which is proved again in the study that the crack formation depth is 51 nm with the cutting depth of 77 nm. Obviously, the dislocation prevails during the cutting process, indicating that DP on basal plane dominates the deformation process. There are 4 DPs, and three of them occur at the time T_i (i=1, 3, 4), as labelled in Fig. 5b. At T_1 (183 ps), the DP 1 forms while both the cutting forces F_x and F_y show no evident changes. However, F_x declines evidently from T_3 to T_4 before the formation of final crack at T_4. A short platform of F_x before T_3 (233 ps) can be observed, which indicates the accommodation of DP 3 to the deformation. Following the formation of DP 4 at T_4 (240 ps), the strain energy rapidly decreases, resulting in an acute decrease of F_x. While

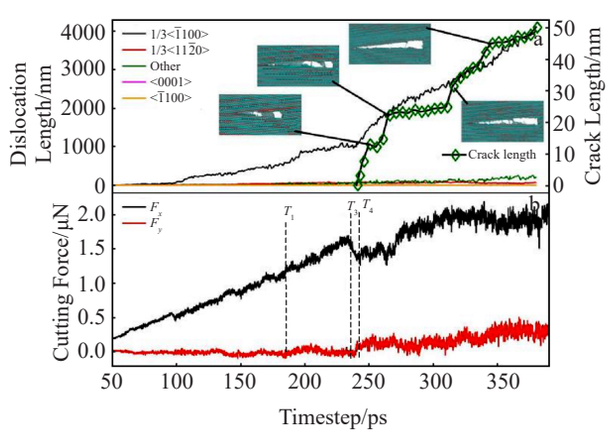

Fig.5 Relationship between timestep and dislocation length and crack length (a); cutting force along X axis (F_x) and Y axis (F_y) (b)

F_y is relatively stable because the deformation process mainly finishes by F_x before T_4, and F_x also contributes to the later deformation process because of the relatively lower decline value of F_x when F_y dominates the deformation process. In addition, F_y increases immediately once the chip remove process needs to be done in the form of crack propagation during the formation of crack at T_4. Then, the pressure of the cutting tool along Y axis increases and F_y increases sharply to support and expand the crack along X axis at T_4. F_x is steady after 20~30 ps therefore, and then F_x increases to about 2 μN to support the crack propagation, and the crack length increases faster.

As shown in Fig.5a, the crack length increases with a similar trend of dislocation length, and circulates with a combination of a rapid increase and a stagnation. The stagnation stage at 255 ps is considered as the result of the connection of a layer of atoms in the opening crack, followed by a long stagnation phase with the connection of a layer of atoms at 265 ps, which lasts for 50 ps until the overall break of the layer of atoms finishes, as indicated in Fig.5a at 315 ps. Finally, the layer of the connected atoms disappears and the dislocation length increases faster. It can be easily concluded that the size effect is considered. The crack expansion goes into stagnation when the crack propagates to an extend with closer crack tip to the fixed boundary, and then the crack expansion decelerates. On the other hand, the opening angle of the crack increases and suffers from an increasing cutting force F_y since the crack forms at 240 ps with the expected deceleration of crack propagation along X axis.

2.2 AE analysis

The median frequency (f_m) and AE power (E) are plotted in Fig.6 at different depth points P_i (i=1, 2, ⋯, 12). The input signal is compressive stress for the analysis with the simulation temperature at 1 K, which suppresses the lattice vibration at room temperature. As a result, most of the f_m points scatter near zero, and the other AE sources can be well distinguished from lattice vibration with higher frequency of f_m. For instance, the single point of f_m around 7700 GHz of P_5 results from the disappearance of atoms by the push force of the moving tool, as shown in Fig.7, and the atoms in the P_5 are pushed away by the cutting tool. Primarily, the common phenomenon in Fig.6 is the decline of AE power in the beginning, and there are mainly two assumptions. The first assumption is that the AE wave is disturbed by the lattice distortion from the dislocation motion, crack formation or cutting tool impact. The sec-

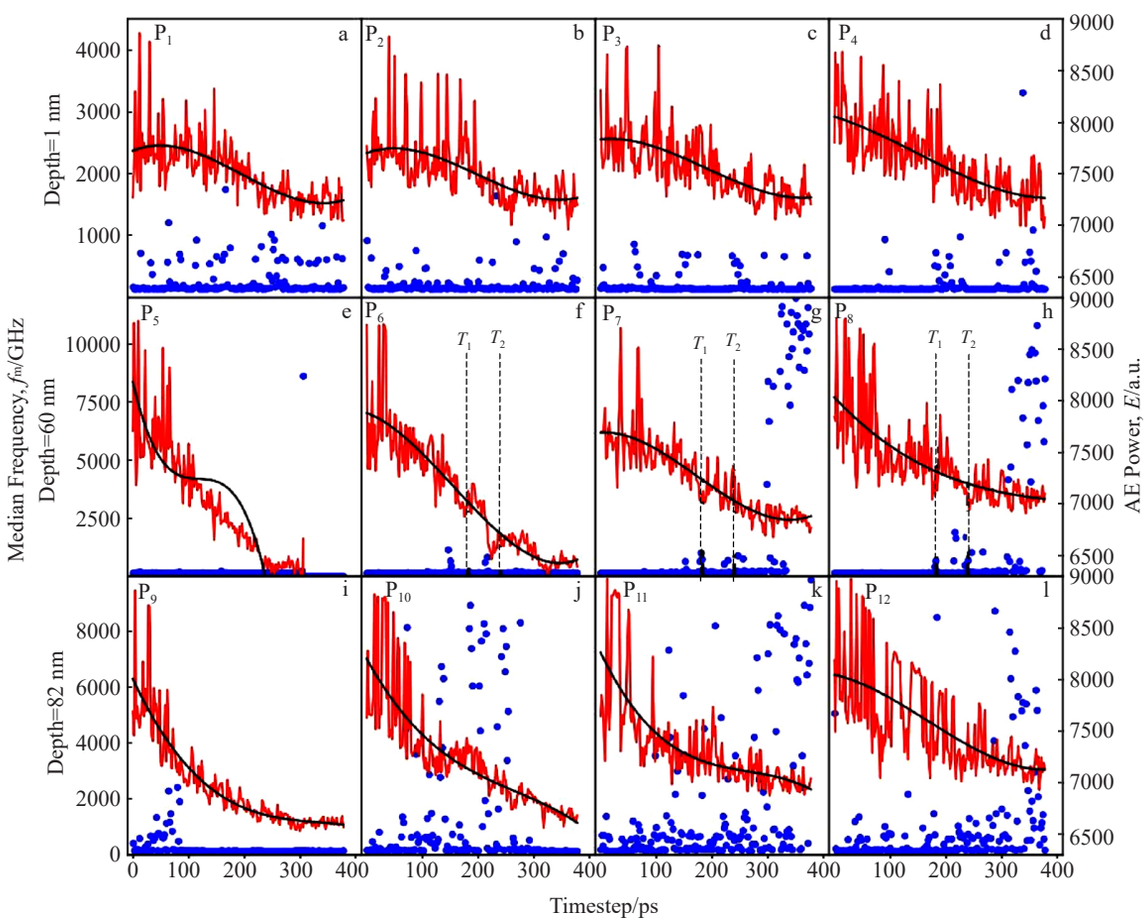

Fig.6 Relationship between median frequency (f_m) and fitted AE power (E) with timestep at different depths: (a~d) 1 nm, (e~h) 60 nm, and (i~l) 82 nm

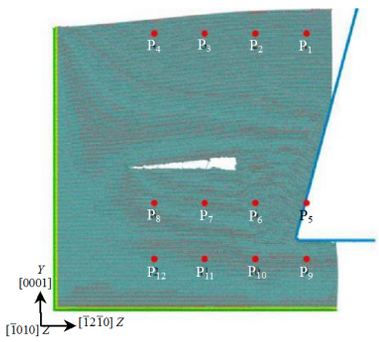

Fig.7 Cutting model at 320 ps during the cutting process

ond assumption is that the compressive stress reduces the averaged distance between atoms and constrains the vibration amplitude of the atoms, which is distinct in these subgraphs. For instance, the points at depth of 60 nm get closer to the cutting tool from P_8 to P_5, which means that the points from P_8 to P_5 suffer a higher compressive stress. Consequently, the decline trend of the fitted AE power curves becomes slower from P_5 to P_8, as well as the trend of AE power curves of the points with the depth of 82 nm. The points with depth of 1 nm are far away from the severely deformed region and seldomly influenced, and the fitted curves without a significant difference and a slighter decline of AE power can be observed, so the slower decline may be caused by not only the latter compressive stress, but also the disturbance of AE wave. Besides, the apparent attenuation of acoustic wave is observed from Fig.6. There are two levels of maximum f_m value fluctuating around 9000 GHz or 4000 GHz, which are shown in Fig.6. The points at depths of 60 and 82 nm locating at upper and lower side of the severely deformed region with approximately equal distance have the same level of f_m maximum value. And the points at the depth of 1 nm are distributed away from the severely deformed region, showing a lower f_m maximum distribution around 4000 GHz.

Apart from the lattice vibration, AE sources also include the DP. As shown in Fig. 6f~6h, the corresponding formation timestep of DP 1 and DP 4 is T_1 (183 ps) and T_2 (240 ps), respectively. These timesteps are the end of formation of each DP, and the DP related AE is already emitted at the beginning. From the view of AE, two valleys of the curve of P_6 located ahead of T_1 and T_2 indicate the beginning of DP 1 and DP 4, respectively. The high frequency f_m points represent DPs accordingly. As the acoustic wave propagates from P_6 to P_7, the acoustic waves from the two DPs arrive with a delay and get closer to T_1 and T_4, respectively. The change of the acoustic wave of P_8 shows the similar trend. So it can be concluded that the DP is one of AE sources and can lower AE power and increase the f_m with the temperature at 1 K.

In comparison with the AE response of DP, the crack propagation has relatively more intense AE characteristics. As shown in Fig.6e~6h, the last part of f_m scatter in Fig.6g and 6h is relatively high, which is considered as the result of crack propagation. On the contrary, as shown in Fig.6f, the last part of f_m gets near to zero, because the crack formation site is behind the point P6. What is more, the high f_m scatter in Fig.6j~6l is obviously not from the crack due to the far away distance and severely compressed atoms, so it is from the plastic deformation near the edge of the cutting tool, which is raised by the break of many bonds under the fierce compressive stress. Furthermore, the high frequency region of f_m varies with the position of cutting tool, and the high frequency region of f_m increases with the increase of cutting tool distance and disappears when the tool moves away.

2.3 Clustering results

Understanding the kinetics of different AE sources with respect to timestep helps to identify and compare them simply and evidently. Especially, the AE events from different AE sources can be figured out, and compared with in-situ observations. The clustering analysis of median frequency (f_m) and AE power (E) distribution is shown in Fig.$8a_1$~$8a_4$, and energy accumulation E_c of each cluster is shown in Fig.$8b_1$~$8b_4$. The formation time of DP 1 and DP 4 at timestep T_1 (183 ps) and T_2 (240 ps) is labeled as well. The clustering procedure of the f_m-E bivariate distribution is partitioned manually, because the number of these points is quite small and the points distribution is easily distinguishable. So a precise clustering of some specific points is necessary. The first AE source colored in black is obviously the lattice vibration, which causes an array of black points scatter corresponding to the lowest f_m, and each E_c of cluster 1 in Fig. $8b_1$~$8b_4$ can be fitted by a curve with the same oblique angle. On the other hand, the single red point in Fig.$8a_1$ results from the disappearance of atoms, giving rise to the platform of blackline in Fig.$8b_1$. There are two other similar platforms in Fig.$8b_3$ and $8b_4$ caused by the disturbance from the third AE source, as indicated by the green lines. Moreover, the deformation process is closely related with phonon, and the relevant phonon frequencies are in the range of 100 GHz to several terahertz at the lattice temperature of a few degrees of Kelvin[37], which agrees with the frequency range in this study.

As shown in Fig.$8a_2$, the other two clusters at P_6 is colored in red and green respectively. The three red points around 7200 GHz and two green points around 6800 GHz of f_m-E scatter are separately clustered although they are from the same AE source. The increased part of E_c of cluster 2 and cluster 3 in Fig.$8b_2$ has a delay with respect to T_1 and T_2, which is similar to the delay at P_6 in Fig.6. All these results indicate that the AE source of cluster 2 and 3 is DP 1 and DP 4, respectively. Then it can be concluded that the AE from one DP can have different f_m with a similar energy level. The f_m-E scatter points from DP 1 and DP 4 at P_7 and P_8 are clustered into the second AE source, which are colored in red, showing a lower frequency of f_m and a gradual increase of E_c during 200~300 ps, and the third AE source colored in green has the highest frequency distribution of f_m and E_c increases dramatically after 300 ps. The AE source forms after the crack formation, and it is considered to be the crack expansion. Furthermore, the crack formation site locates behind the points P_5 and P_6, which means

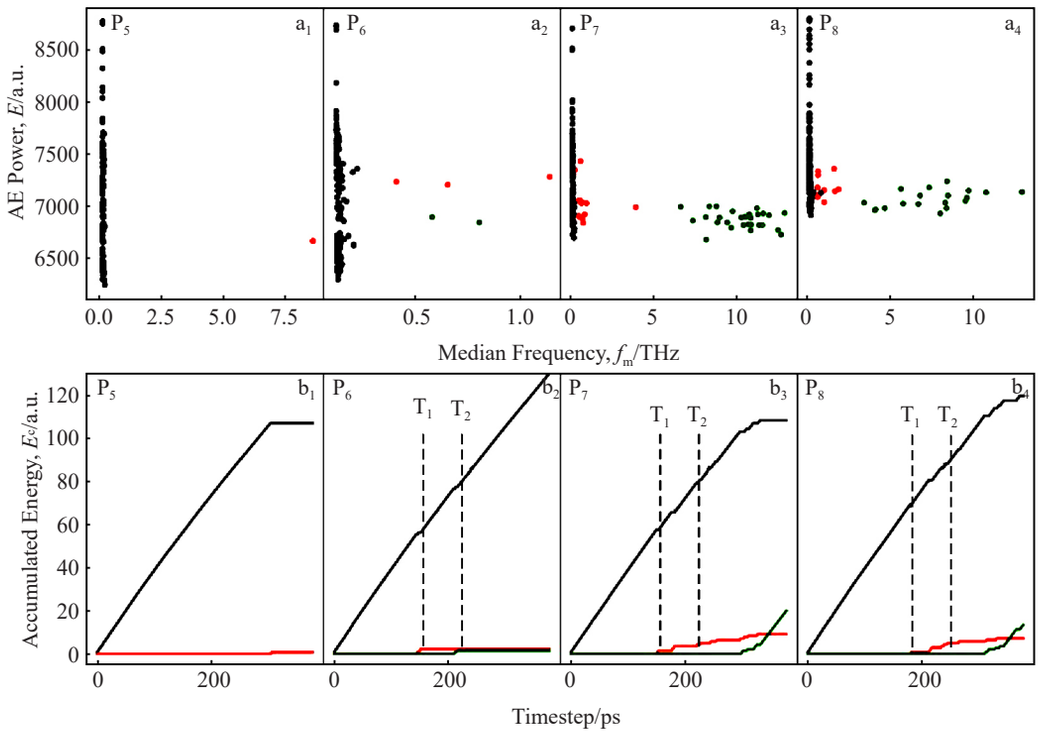

Fig.8 Cluster analyses of the median frequency (f_m) and AE power (E) bivariate distribution (a_1~a_4), and energy accumulation (E_c) of each cluster (b_1~b_4) at different points: (a_1, b_1) P_5, (a_2, b_2) P_6, (a_3, b_3) P_7, and (a_4, b_4) P_8 (cluster 1-black; cluster 2-red; cluster 3-green)

that the influence of crack expansion on AE of the two points is weak. What' s more, the wave propagation process also can be seen in Fig.8b_2~8b_4. For example, the increasing energy point of E_c curve in red at the beginning in Fig.8b_2, and the corresponding delays from P_6 to P_8 all indicate the propagation time of AE wave from DP, as well as the third AE source colored in green.

As reported by Vinogradov et al[38] in the typical picture of AE power and median frequency at room temperature, the AE power peaks at the beginning of plastic yielding, and then drops gradually. In this study, it is the similar case, as shown in Fig. 6. The elastic deformation is nearly unobservable because the DP 1 forms during the initial contact between the tool and workpiece. Then the plastic deformation begins from DP 1 to DP 4, and T_1 and T_2 in Fig.6 and Fig.8 correspond to DP 1 and DP 4, respectively, indicating that the plastic deformation can be observed from AE sources of DP. At last, the brittle deformation begins during the formation of final crack. The related AE responses are not only the slightly increasing f_m distribution at P_7 and P_8 in Fig. 6, but also the increasingly accumulated AE power energy in green at P_7 and P_8 in Fig.8.

3 Conclusions

1) Under high compressive stress, the dislocation propagations (DPs) along $-X$ axis is likely to occur. Consequently, four times of DPs divide the deformed workpiece ahead of the tool into several pieces, and each piece does not undergo the plastic deformation. With the increase of cutting distance, the compressive stress from the tool compresses each piece into amorphous state.

2) The crack begins with a fast DP near the nose of the cutting tool to the front, which reduces cutting force F_x sharply, and F_y increases sharply during the formation of the crack. In addition, the crack length circularly increases with a stage of stagnation, and the expanding rate of crack length decelerates at the end of cutting because of the size effect.

3) Three acoustic emission (AE) sources including lattice vibration, DP and crack propagation are derived from the cutting process. The low temperature constrains the vibration of atoms, and it has the lowest median frequency (f_m) distribution. The crack propagation has a relative higher level for accumulated energy of AE power (E) and median frequency distribution. The f_m-E analysis indicates that the lattice vibration still occupies a large proportion in the energy accumulation during the cutting process. Besides, the attenuation of AE wave can be observed from the data collecting points.

4) Compared with the lattice vibration, DP increases the median frequency but decreases the AE power. For the same one DP, the f_m frequency scatter is different but has the same energy level of AE power.

5) The initial decline of AE power results from the compressive stress from interaction between the tool and workpiece, which constrains the amplitude of lattice vibration and reduces the AE power consequently. The subsequent decline of AE power results from not only the compressive stress, but also the dislocation activities and crack propagation. In addition, the reflection of AE near the free surface and fixed boundary leads to the oscillation of AE power with a general higher me-

dian frequency values.

References

1 Zhang J G, Cui T, Ge C *et al*. *International Journal of Machine Tools and Manufacture*[J], 2016, 106: 109
2 Xiao L L. *International Journal of Machine Tools and Manufacture*[J], 2020, 42(2): 157
3 Deschanel S, Rhouma W B, Weiss J. *Scientific Reports*[J], 2017, 7(1): 1
4 Lee S H, Ahn B W. *Key Engineering Materials*[J], 2006, 326-328: 405
5 Alberto C, Giuseppe L. *Acoustic Emission and Critical Phenomena*[M]. London: Taylor & Francis, 2014
6 Vinogradov A Y, Merson D L. *Low Temperature Physics*[J], 2018, 44(9): 930
7 Eshelby J D. *Physical Review*[J], 1953, 90(2): 248
8 Merson D, Nadtochiy M, Patlan V *et al*. *Materials Science and Engineering A*[J], 1997, 234: 587
9 Hora P, Machová A, Červ J *et al*. *Kovove Materialy*[J], 2019, 57(2): 75
10 Anderson P M, Hirth J P, Lothe J. *Theory of Dislocations*[M]. New York: Cambridge University Press, 2017
11 Vinogradov A, Vasilev E, Linderov M *et al*. *Materials Science and Engineering A*[J], 2016, 676: 351
12 Zhu Y T, Liao X Z, Wu X L. *Progress in Materials Science*[J], 2012, 57(1): 1
13 Müller A, Segel C, Linderov M *et al*. *Metallurgical and Materials Transactions A*[J], 2015, 47(1): 59
14 Nikonov A, Zharmukhambetova A. *AIP Conference Proceedings* [J], 2018, 2051: 20 215
15 Saurav G. *Journal of Physics D, Applied Physics*[J], 2014, 47(24): 243 001
16 Xiao G B, To S, Zhang G Q. *Computational Materials Science* [J], 2015, 98: 178
17 Meng B B, Zhang F H, Li Z P. *Materials Science in Semiconductor Processing*[J], 2015, 31: 160
18 Meng B B, Yuan D D, Xu S L. *Nanoscale Research Letters*[J], 2019, 14(1): 1
19 Li Ruixiang, Zhou Wei, Ran Guang *et al*. *Rare Metal Materials and Engineering*[J], 2018, 47(1): 378 (in Chinese)
20 Xiao G B, To S, Zhang G Q. *International Journal of Nanomanufacturing*[J], 2015, 11(1-2): 64
21 Noreyan A, Amar J G, Marinescu I. *Materials Science and Engineering B*[J], 2005, 117(3): 235
22 Noreyan A, Amar J G. *Wear*[J], 2008, 265(7-8): 956
23 Yan J, Zhang Z Y, Kuriyagawa T. *International Journal of Machine Tools and Manufacture*[J], 2009, 49(5): 366
24 Geng Ruiwen, Yang Xiaojing, Xie Qiming *et al*. *Rare Metal Materials and Engineering*[J], 2019, 48(8): 2544 (in Chinese)
25 Lee S H. *International Journal of Machine Tools and Manufacture*[J], 2012, 61: 71
26 Osipiyan Y A, Smirnova I S. *Phys Status Solidi B*[J], 1968, 30(1): 19
27 Nguyen T D, Plimpton S J. *Computational Materials Science*[J], 2015, 100: 173
28 Zhou M. *Proceedings of the Royal Society of London. Series A: Mathematical Physical and Engineering Sciences*[J], 2003, 459 (2037): 2347
29 Egami T. *Progress in Materials Science*[J], 2011, 56(6): 637
30 Rycroft H C. *Chaos*[J], 2009, 19(4): 41 111
31 Vashishta P, Kalia R, Nakano A *et al*. *Journal of Applied Physics* [J], 2007, 101(10): 103 515
32 Jeng Y R, Tsai P C, Fang T H. *Tribology Letters*[J], 2005, 18(3): 315
33 Tersoff J. *Phys Rev B*[J], 1988, 37(12): 6991
34 Guo W Z, Peng Z, Xuan C J*et al*. *Phys Rev B*[J], 2015, 64(19): 198 014
35 Stukowski A. *Modelling Simul Mater Sci Eng*[J], 2010, 18(1): 15 012
36 Stukowski A, Bulatov V V, Arsenlis A. *Modelling & Simulation in Materials Science & Engineering*[J], 2012, 20(8): 85 007
37 Wolfe J P. *Imaging Phonons: Acoustic Wave Propagation in Solids*[M]. New York: Cambridge Press, 2000
38 Vinogradov A, Yasnikov I S, Estrin Y. *Journal of Applied Physics* [J], 2014, 115: 233 506

6H-SiC脆性切削声发射响应的分子动力学研究

冯瑞成[1,2]，祁永年[1,2]，李海燕[1,2]，宋文渊[1,2]，樊礼赫[1,2]，雷春丽[1,2]，冯国金[3]，芮执元[1,2]

(1. 兰州理工大学 机电工程学院，甘肃 兰州 730050)

(2. 兰州理工大学 数字制造技术与应用省部共建教育部重点实验室，甘肃 兰州 730050)

(3. 哈德斯菲尔德大学 效率与效能工程中心，英国 哈德斯菲尔德 HD1 3DH)

摘　要采用分子动力学方法研究了6H-SiC脆性切削的声发射响应。研究了原子尺度下6H-SiC的微变形和裂纹形核，同时对加工过程中的声发射源进行了识别，分析了其相应的声发射特征。结果表明，6H-SiC在77 nm切削深度下的脆性变形过程简单但不寻常；在6H-SiC切削过程中位错不会连续扩展，变形后的工件在刀具挤压作用下被分割成块，并由位错的快速扩展引发裂纹。对于影响声发射源特征的因素研究发现：初始压应力会导致声发射功率的下降；频率-能量分析中可见的3种声发射源分别是晶格振动、位错扩展和裂纹扩展。此外，在1 K温度下，2次明显的位错传播的声发射响应比晶格振动具有更高的频率特性，但总能量水平最低。相反地，裂纹扩展的声发射响应具有更为明显的频率分布特性和能量特性。

关键词：声发射；脆性加工；6H-SiC；分子动力学

作者简介：冯瑞成，男，1976年生，博士，副教授，兰州理工大学机电工程学院，甘肃 兰州 730050，E-mail：postfeng@lut.edu.cn